Available online at www.sciencedirect.com
ScienceDirect
Cement and Concrete Research 37 (2007) 1265–1277
Cement and Concrete Research

Characterization of elastic and time-dependent deformations in normal strength and high performance concrete by image analysis

Mauricio Lopez [a], Lawrence F. Kahn [b], Kimberly E. Kurtis [b,*]

[a] School of Engineering, Pontificia Universidad Católica de Chile, Av Vicuña Mackenna 4860, Casilla 306, Correo 22, Santiago, Chile
[b] School of Civil and Environmental Engineering, Georgia Institute of Technology, 790 Atlantic Dr. NW, Atlanta, Georgia 30332-0355, USA

Received 22 August 2006; accepted 25 May 2007

Abstract

Deformations in normal strength concrete (NSC) and high performance concrete (HPC) were examined using image analysis to better understand the distribution of strain in these materials as related to their composition and microstructure. Elastic strain, creep and shrinkage were shown to occur non-uniformly throughout the NSC and HPC microstructure and creep and shrinkage strain both increased with time, as expected. The non-uniformity in the strain measurements also increased with time, as a consequence of dissimilarities in time-dependent behavior of the paste and the aggregate. However, compared with NSC, the time-dependent strains in the HPC were lower and showed less variation, suggesting a more uniform microstructure. In both NSC and HPC, high-strain sub-regions were evident in the vicinity of the interfacial transition zone (ITZ), likely as a consequence of the strain mismatch between aggregate and paste. The thickness of the high strain sub-regions along the ITZ in HPC were approximately one half of those in NSC.

Keywords: Aggregate; Cement paste; Creep; Interfacial transition zone; Shrinkage

1. Introduction

A number of theories, mechanisms, and empirical models have been proposed over the years to describe creep and shrinkage in concrete [1–4]. Some can adequately explain and predict creep and shrinkage of normal strength concrete (NSC) under various conditions, but interest remains in improving the understanding of the fundamental mechanisms of creep and shrinkage. In addition, the introduction and widespread acceptance of high performance concrete (HPC) – with its lower water-to-cementitious materials ratio (w/cm), use of supplementary cementitious materials (SCMs), and denser, more refined, and more uniform microstructure – has lead to renewed interest in understanding the practical and fundamental aspects of deformation in this type of concrete.

Traditionally, deformations in concrete have been examined in a "bulk" sense, where deformations occurring in the different phases (i.e., paste, aggregate and interfacial transition zone — ITZ) are considered together in an overall measurement of strain. While the "bulk" characterization of deformation has been useful for design purposes, this methodology does not provide enough information to understand the mechanisms of creep and shrinkage at a fundamental level.

Image analysis can be used to measure deformation and to map the distribution of deformation in a sample by comparison of a series of images obtained for same region of interest (ROI). In this way, information about the distribution of deformation in the phases forming the composite (i.e., matrix or paste fraction, aggregate, and ITZ) and the interactions between those phases over time (or with increasing stress, drying, etc.) can be obtained. Measurements of deformation using image analysis in concrete under monotonically increasing mechanical stress [5,6] and under environmental stress [7,8] have been made, but creep in concrete has not been previously examined using such techniques.

Because this technique allows deformation to be visualized and linked to specific microstructural features, such as aggregate, paste, voids, and ITZ, image analysis can provide

* Corresponding author. Tel.: +1 404 385 0825; fax: +1 404 894 0211.
E-mail address: kkurtis@ce.gatech.edu (K.E. Kurtis).

0008-8846/$ - see front matter © 2007 Elsevier Ltd. All rights reserved.
doi:10.1016/j.cemconres.2007.05.011

additional insight into the mechanisms of deformation not available with more traditional measurements. The objective of this research, then, is to use image analysis to characterize deformation in cement-based composites, including NSC and HPC, to provide new insight into the processes of creep and shrinkage and how these processes differ in NSC and HPC. Specifically, in this research, image analysis, performed by digital image correlation, was used to map elastic and time-dependent deformations and to assess relative deformations in the different phases, while the material remained under sustained load and drying. A new experimental setup was developed to cast, load, and image the surface of concrete specimens, and a commercially available software package was adapted to perform the analysis [9–11].

2. Overview of creep in NSC and HPC

Creep in concrete has been systematically studied for almost a century. Troxell et al. [12] measured creep and shrinkage for over 20 years in concretes with compressive strength between 13.8 and 27.6 MPa (2000 and 4000 psi). Depending of the aggregate type, specific creep (creep divided by the applied stress) when loaded at 28 days of age measured between 109 and 267 με[1]/MPa (0.75 and 1.84 με/psi), with most of values in a narrower range between 160 and 225 με/MPa (1.10 and 1.55 με/psi). Shrinkage after 20 years was found to vary widely as well, with values between 500 and 1300 με. The authors [12] concluded that aggregate played a fundamental role in restraining the time-dependent deformations of the paste. In fact, Pickett [13] and Neville [14] among others, proposed models for creep and shrinkage, based on the deformations of the cement paste and the volume and mechanical properties of the aggregate.

One-year specific creep for HPC with compressive strength of 70 MPa (10,150 psi) and higher which was loaded at 28 days of age was reported by de Larrard et al. [15] to be in the range of 15 to 65 με/MPa (0.10 to 0.45 με/psi), with most of the results in the 20–40 με/MPa (0.14–0.28 με/psi) range. These results are approximately 10–25% of the values reported for NSC in [12], showing a remarkable reduction in creep of HPC. Dilger and Wang [16] concluded that after several years, deformation in NSC was normally two to four times the elastic deformation, giving a creep coefficient of 2 to 4. In contrast, the creep coefficient for HPC was determined to be in the range 1.8 to 2.4. While noting that creep in NSC and HPC are generally affected by the same parameters in similar ways, the lower creep observed in HPC was ascribed to its lower w/cm and the use of silica fume. Other researchers [16–18] have concluded that the main difference between creep in NSC and HPC may be attributed to the significantly lower drying creep observed in HPC. Buil and Acker [17] reported similar conclusions for shrinkage; i.e., the reduction in total shrinkage of HPC with respect to NSC is due to the lower drying shrinkage of HPC.

Thus, the understanding of the variations in creep and shrinkage deformation in HPC relative to NSC remain unresolved and warrant further investigation to understand, at a fundamental level, both the relationship between creep and shrinkage and the influence of mixture proportions and material constituents.

[1] με indicates a measurement made in microstrains (mm/mm × 10^{-6} or in/in × 10^{-6}).

3. Experimental approach

3.1. Method

A new experimental setup was developed which consisted of a reduced size, permanently loaded specimen, which is indexed such that specific specimen locations could be observed and imaged over time. The test setup, shown in Fig. 1a and b, consists of an unbonded post-tensioned system, where an internal 862-MPa (125-ksi) yield strength steel threaded rod is placed in tension, and the prismatic cement-based specimen remains under compression. This setup was developed using the guidelines provided by ASTM C 512 [19], but 38 × 38 × 125 mm (1.5 × 1.5 × 5 in) prismatic specimens are used instead of 150 × 300 mm (6 × 12 in) cylindrical specimens. As required by ASTM C 512 [19], after initial curing, the specimens were dried at 50% relative humidity and 23 °C (73 °F). The prismatic shape was required to provide a flat surface for microscope viewing and to give an undistorted image with an adequate depth of field.

For this research, specimens were cast in pairs. The specimens were cast such that each prism, when cut (as described next), would contain a cast-in 12.7-mm (0.5-in) center hole in the longitudinal direction, which allowed the steel tension rod to pass through without contact or bonding. After demolding, the single cast sample was cut in two with a diamond saw to eliminate edge effects and to expose the aggregate. The cut surfaces were then polished using 120, 240, 360, and 600 silicon carbide (SiC) grit to obtain a suitable surface for imaging. A sample held in the test frame and its geometry are shown in Fig. 1, and Fig. 2 shows the experimental setup. Companion specimens of the same type of mixture were cast, monitored, but not loaded in order to measure the environmental stresses (drying shrinkage and thermal strains) as recommended by ASTM C 512 [19].

In this test frame (Fig. 1), a compressive load equivalent to a stress of 40% of the compressive strength of the specimen, as recommended by ASTM C 512 [19], is applied through the rod with a center hole hydraulic jack (which can be attached to the top loading plate) and is transmitted to the loading plate in the middle through the disk springs. That second loading plate transfers the applied load to the specimens, which finally transmits the load to the bottom loading plate and bottom nut. Once the top nut is tightened, the threaded rod remains in tension while the rest of the frame and concrete specimen remain in compression. The disk springs help to maintain the load while the specimen contained in the frame undergoes creep and shrinkage. In this research, the frames were reloaded periodically to minimize the stress losses of the system assuring they were not higher than 5% of the initially applied stress. This was measured with a load cell placed between the frame and the hydraulic jack. In addition to deformation data acquired by the strain mapping technique, “bulk” measurements of deformation

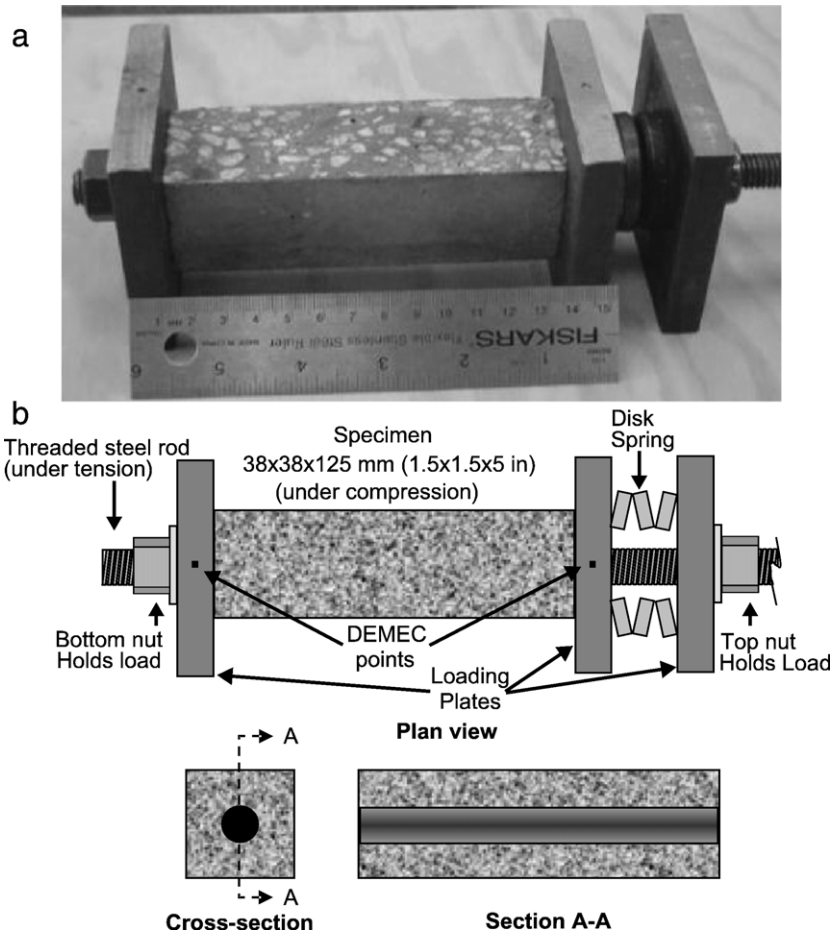

Fig. 1. Experimental setup: loading frame.

were made on samples in the frame with a detachable mechanical (DEMEC) gauge.

3.2. Image analysis computational procedure

A small-scale sample, held in a creep frame, is shown in Fig. 2 sitting in the indexible stage of the stereomicroscope while an image is acquired. Fig. 2 also shows the image acquisition system comprised of the stereomicroscope, 2-megapixel digital camera, computer (with imaging software) and monitor. The microscope stage allows for precise re-positioning of the creep frames such that image coordinates, corresponding to regions of interest (ROIs) can be re-imaged over time.

3.2.1. Imaging procedure

For each sample, four ROIs were selected, to obtain images which each capture the aggregate, paste, and ITZ, using two levels of magnification. The two levels of magnification selected correspond to the maximum and minimum attainable with the microscope configuration, and the two levels were used to compare strain maps at different magnifications.

At the lower magnification, one pixel represents 5.92 μm (2.3×10^{-4} in) which roughly corresponds to 12.6× magnification, when viewed through the eyepieces. At the higher magnification, one pixel represents 1.08 μm (4.2×10^{-5} in), which is equivalent to 80× magnification as seen through the eyepieces. Images of 1600×1200 pixels were acquired. Thus, images of each ROI were either 0.673 cm^2/9472 μm×7104 μm (0.104 in^2/0.373 in×0.280 in) at low magnification or 0.022 cm^2/1728 μm×1296 μm (0.003 in^2/0.068 in×0.051 in) at high magnification. Fig. 3 shows a schematic of the specimen surface, the ROIs at the two magnification levels and the coordinate system. In order to minimize boundary effects from the loading plates, all ROIs were located more than 38 mm (1.5 in) away from the specimen ends.

3.2.2. Pattern matching procedure

A pattern matching procedure was applied to different image pairs from the same ROI at different states of deformation. Commercially available software with pattern recognition capabilities was used [20]. Each pair of images had a "reference image" (REF) and a "deformed image" (DEF). A C-code was written to iteratively perform the software's pattern recognition through the images. The algorithm, initially applied to the pixel (100, 100) from the top-left edge, had the following four steps:

1) In REF, a 65×65 pixel area with the pixel of interest at its center is selected. This sub-region is called reference window.
2) In an output file, the coordinates of the pixel of interest in REF are recorded.

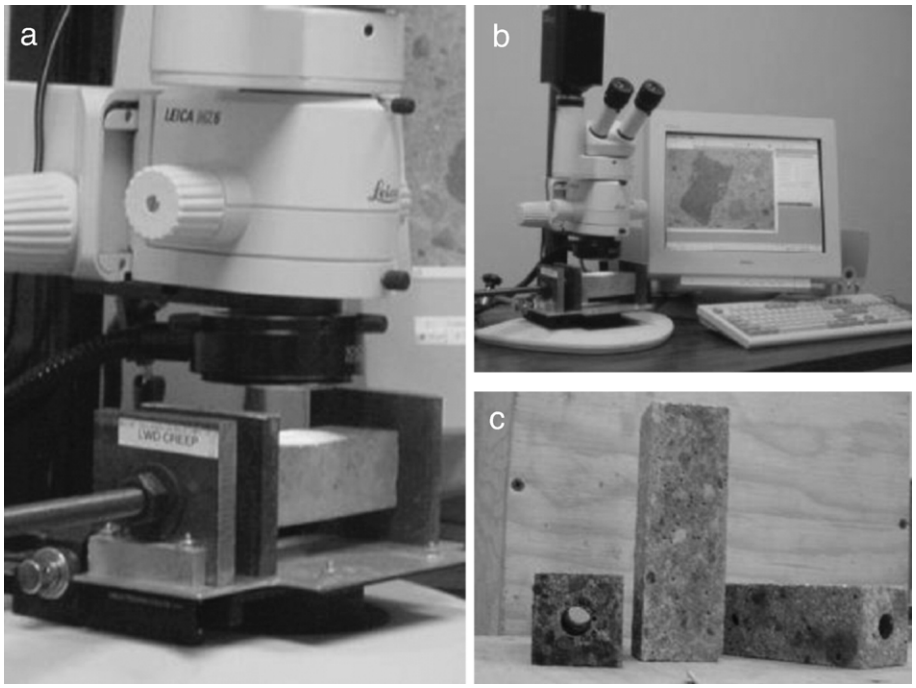

Fig. 2. (a) Experimental setup, creep frame and specimens in the stereomicroscope stage, (b) image acquisition system, and (c) concrete specimens after cutting and polishing.

3) In DEF, the pixel of interest and its neighbors (reference window) are located.
4) In the output file, the coordinates of the pixel of interest in DEF are recorded.

After recording the coordinates of the pixel of interest in REF and DEF, the algorithm moved to the following pixel, located 15 pixels away from the previous one, and the series of steps was repeated until completing the ROI. In order to fit the reference window and to allow for some inadvertent shifting between image pairs, the 100-pixel edge is not considered during the matching procedure. As a result, the actual matching area is 1400 × 1000 pixels.

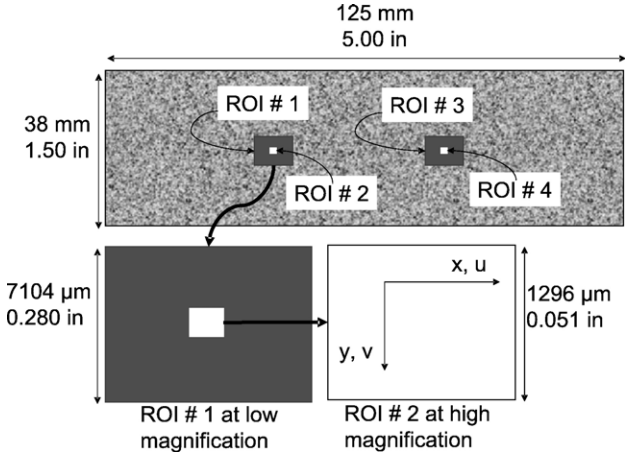

Fig. 3. Imaging protocol for the experimental program.

The pattern matching/recognition procedure used was a trial-and-error algorithm that performed a numeric comparison between the reference window from REF and a candidate subregion from DEF. A "similarity score" was obtained and compared against a threshold value. If the score was lower than the threshold, a new candidate was evaluated. If the score was greater than the threshold, the matching was complete. The algorithm is able to interpolate among pixels to find the best match, so it can give an accuracy of 0.01 pixels (i.e., 0.01 µm at high magnification and 0.059 µm at low magnification). One difficulty in using a threshold value is that images always contain some "noise" (e.g., slight variations in lightning or focus), which can lower the similarity scores of the candidate regions. Overly high thresholds might lead to rejection of a correct match and may even lead to unmatched pixels. On the other hand, threshold values which are too low may lead the acceptance a good candidate, even though it is not the correct match. Consequently, the output file from the pattern matching procedure may contain unmatched pixels that must be reassessed as well as wrong matches that must be filtered out, as described next.

3.2.3. Displacement and strain calculation

The output file produced during ROI matching was further processed to compute displacements and strain. This post-processing was performed automatically (using another algorithm especially written for this purpose) in three stages: (1) displacement computation, (2) displacement filtering, and (3) strain computation.

Displacements were calculated in the X and Y directions and were denoted, by convention, as u- and v-displacements, respectively (see Fig. 3 for coordinate reference system). The

u-displacements were calculated as the difference between the *X*-coordinates of the same pixel from DEF and REF. Likewise, *v*-displacements were the difference between *Y*-coordinates of a pixel on each of the images. Whenever an unpaired pixel was found, the displacement was assumed to be a very large number, so that the pixel could be subsequently filtered.

The filtering stage aimed to eliminate the incorrect matches and to fill in the unmatched pixels. Chauvenet's criterion is a commonly used statistical technique that allows for discrimination of outliers in a data set [21,22]. It computes the average and variance of a data set and then the deviation of any particular data point from the average. If the deviation is higher than a particular threshold, the data point is said to be an outlier. For this case, the data set was comprised of the displacement of a pixel and those of its eight nearest matched neighbors. If that pixel was an outlier according to Chauvenet's criterion, its value was replaced by the average of those eight neighbors. Because the displacements of the unpaired pixels were assumed to be very large, they were always classified as outliers by the Chauvenet's criterion.

After the displacements were filtered, strain was computed as the relative displacement between two adjacent pixels divided by the initial 15-pixel distance between them. Thus, the difference in *u*- and *v*-displacements between two pixels divided by 15 (i.e., initial distance between matched pixels, as described in Section 3.2.2) was called strain in *X*- and *Y*-direction, respectively.

Table 1
Design, kg/m^3 (lb/yd^3), and strength, MPa (psi) of the NSC and HPC mixtures

	NSC	HPC
Type I cement	319 (537)	–
Type III cement	–	442 (745)
Silica fume	–	59 (100)
Class F fly ash	–	89 (150)
Water	188 (317)	135 (228)
Natural siliceous sand (FM=3.15)	845 (1424)	611 (1030)
9.5 mm (0.375 in) MSA granite	963 (1623)	987 (1664)
Water reducer (WRDA) 35[a]	–	2.7 (4.6)
High range water reducer (ADVA flow)[b]	–	5.9 (9.9)
Air entraining agent (Daravair 1000)[c]	–	0.3 (0.5)
Water-to-cementitious materials ratio (w/cm)	0.60	0.23
Cement paste content by volume (%)	29	39
Coarse/fine ratio by volume	1.07	1.5
Theoretical density kg/m^3(lb/ft^3)	2355 (147)	2340 (146)
1-day cylinder compressive strength MPa (psi)	8.6 (1250)	80.4 (11,660)
28-day cylinder compressive strength MPa (psi)	25.8 (3740)	96.6 (14,005)
Compressive strength, cubic specimens MPa (psi)	24.5[d] (3550)	77.0[e] (11,165)
Compressive strength, prismatic specimens MPa (psi)	21.1[d] (3065)	67.8[e] (9835)
Stress applied to creep specimens	9.7 (1410)	28.4 (4115)

[a]0.45% of cementitious materials by weight.
[b]1.0% of cementitious materials by weight.
[c]0.05% of cementitious materials by weight.
[d]obtained at 28 days age.
[e]obtained at 24 h age.

3.3. Testing program

The mixture designs for the NSC and HPC are shown in Table 1. The NSC mixture design was the same as that from Troxell et al. [12], with the main difference being that the maximum size aggregate (MSA) was reduced to 9.5 mm (0.375 in) for use in the devised test setup. The HPC mixture design used is typical of a high performance low w/cm concrete. This mixture contains 590 kg/m^3 (995 lb/yd^3) of cementitious materials, including Type III portland cement, 10% of silica fume and 15% of class F fly ash. As with the NSC, MSA of the HPC mixture was 9.5 mm (0.375 in).

Six 50.8-mm (2-in) cubic and six 38×38×125 mm (1.5×1.5×5 in) prismatic specimens, with cast-in center hole, were cast from a single batch of each mixture. Because, the HPC mixture was designed to develop high strength at early ages, such as would be required in the precast and prestressed industries, the mechanical testing and creep and shrinkage testing was initiated at 24 h of age. The NSC testing was initiated at 28 days, which is the standard age for testing.

Compressive strength of three 50.8-mm (2-in) cubic and three 38×38×125 mm (1.5×1.5×5 in) prismatic specimens, with cast-in center hole, was measured according to ASTM C 109 [23] at the age of 24 h for HPC and 28 days for NSC. HPC had a 24-hour cube compressive strength of 77.0 MPa (11,165 psi) while NSC had a 28-day cube compressive strength of 24.5 MPa (3550 psi). The cube compressive strength was on average 16 and 14% higher than that measured on the prisms, for the NSC and HPC, respectively (Table 1). This difference is likely due to the larger height-to-width ratio of the prismatic specimens. In addition, three 150×300-mm (6×12 in) cylindrical specimens were tested for compressive strength at the age of 24 h and 28 days according to ASTM C192 [24]. The NSC strength at one and 28 days was 8.6 MPa (1250 psi) at 24 h and 25.8 MPa (3740 psi) at 28 days. The HPC strength was 80.4 MPa (11,660 psi) at 24 h and 96.6 MPa (14,005 psi) at 28 days.

Prismatic creep and shrinkage specimens were placed in the small-scale frames, and the former were loaded to approximately 44% of their ultimate strengths, as shown in Table 1. NSC specimens were loaded at 28 days of age while HPC specimens at 24 h of age; this loading regimen was selected to match prior research on these mixtures [12,25,26] but is also representative of common field loading conditions (i.e., where sustained loading would be applied earlier to HPC concrete).

Digital images and DEMEC readings were obtained immediately before and after loading and, subsequently, after one and 28 days under loading and drying, according to ASTM C512. The companion shrinkage specimens were installed in a similar frame, but remained unloaded, and images and DEMEC reading were obtained at the same intervals.

Data acquired from the loaded specimens included elastic, creep and shrinkage deformations. The elastic portion was captured between the measurements before and immediately after loading. Creep plus shrinkage was obtained from the changes between measurements immediately after loading and those after one or 28 days under loading. Additionally, for the

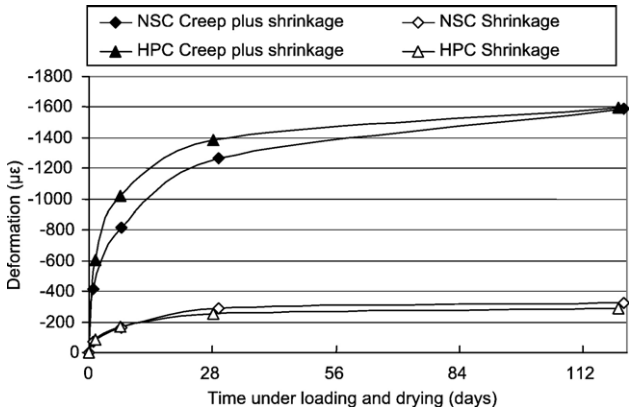

Fig. 4. Time-dependent deformation measured using DEMEC gauge on NSC and HPC specimens.

DEMEC readings, creep and shrinkage could be separated by subtracting shrinkage measured on the non-loaded specimens from creep plus shrinkage obtained in the loaded specimens.

4. Results and discussion

Before using the pattern matching system to measure deformations, data were collected during rigid body motion and analyzed to assess the variability and possible error in the pattern matching algorithm. Two images of the same ROI were obtained before and after displacing the specimen on the indexible stage in order to obtain pure rigid body motion. The variation between maximum and minimum displacements, at high magnification, was 0.9 pixels or less than 1 μm (4×10^{-5} in), but 99% of the pixels displaced within only 0.3 pixels (0.32 μm or 1.3×10^{-5} in), as presented in greater detail in [10]. This confirmed that the proposed method was able to track displacements accurately.

4.1. Comparison of "bulk" strain and strain obtained by image analysis

As described in the experimental approach, measurements of bulk strain in the NSC and HPC samples were obtained by DEMEC readings every time the ROIs were imaged. Fig. 4 presents the deformation measured over time for the loaded specimens (creep plus shrinkage) and the non-loaded specimens (shrinkage), for the two types of concrete. It should be noted that even though the creep plus shrinkage and shrinkage deformations were similar in NSC and HPC, the HPC sample was loaded at the age of 24 h rather than the 28 days of the NSC sample.

The experimental method allowed for comparison between strain measured at the surface by image analysis and those measured by DEMEC gauge considering the entire specimen. The elastic, creep and shrinkage deformations as measured by DEMEC gauge compared to average strains obtained by image analysis are shown in Fig. 5, where the diagonal dashed line represents the equivalence between strains obtained by the two measures. From this comparison, which considers both NSC and HPC, the average strain determined by image analysis is approximately 30% lower than that measured with the DEMEC gauge. However, the strains from pattern matching and DEMEC do follow the same trends, validating the principle of the measurements made by image analysis. In some particular ROIs, the differences in the measurements were within 5%.

The difference observed between the bulk and localized strain measurements is believed to be caused by the limited number of ROIs examined (due to computational constraints) and the selection of the ROIs. That is, the ROIs selected were not chosen randomly. Rather, they were purposely selected such that paste, aggregate, and ITZ would be present to facilitate the objectives of this research. As a result, the images generally contained relatively less paste than the actual volume fraction in the mixtures, and because creep and shrinkage occur largely in the paste, the images showed consistently lower strains than bulk measurements. Future research may, instead, rely on random selection of ROIs, and the examination of a greater surface area of the sample by image analysis.

The difference in the two strain measurement methods, however, is not believed to be related to the consideration that the image analysis is performed on data obtained at the surface, while the bulk measurements represent the sample volume. A previous investigation [5] compared strains obtained with pattern matching, using surface data, and X-ray microtomography, using volumetric data. Those researchers found a strong correspondence between strains measured at the surface and in the volume of mortar and concrete specimens under elastic deformations.

4.2. Deformation in NSC

4.2.1. Elastic strain in NSC

Fig. 6 shows a representative region of interest (ROI) at high magnification and the map of displacement, obtained in the loading direction (*X*-direction), for the NSC specimen. This analysis was performed on images obtained just prior to and just after the application of a 9.7 MPa stress, and, hence, captured elastic deformation. However, it should be noted that the displacement field, in Fig. 6b, includes not only the deformation due to the applied load but also some unavoidable rigid body

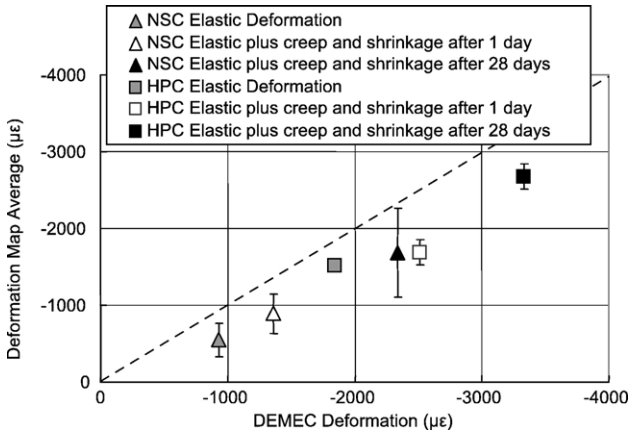

Fig. 5. Total strain as measured by DEMEC gauge versus average total strain from strain maps.

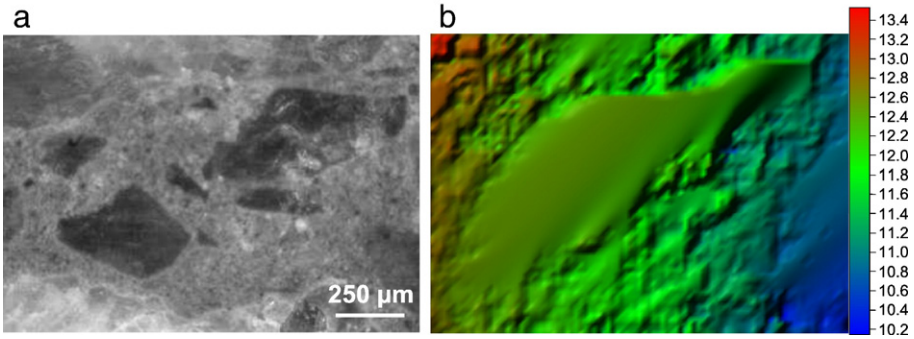

Fig. 6. (a) A representative region of interest (ROI 4), obtained at high magnification on an NSC specimen under 9.7 MPa (1440 psi) stress. (b) map showing u-displacement field, in number of pixels.

motion due to shifting of ROI between the to images. The displacement field resulted in only positive displacement values in the scale bar. According to the coordinate system selected, the positive sign in displacements indicates that pixels are moving to the right of the picture. From Fig. 6b it can be seen that the pixels on the left have higher values than those on the right. This indicates that the pixels on the left are getting closer to those on the right or, more specifically, that this region is under compression, as expected. In addition, the presence of two larger aggregate particles (located near the center of the ROI) could have locally distorted the displacement field. Overall, these data demonstrate the dependence of the strain field on the microstructure and phase distribution within the concrete, as modeled previously by Bremner and Holm [27].

Fig. 7a shows a representative ROI at high magnification and Fig. 7b the elastic strain map of that ROI due to the applied stress.

The strain map in Fig. 7b shows that non-uniform strain field has developed as a consequence of the NSC's heterogeneous microstructure, as previously observed [5,6]. The strain map for this ROI (Fig. 7b) presents a wide range of deformations from −10,000 με in compression [indicated by blue in the scale for color images (electronic version) and black for grayscale images (print version)] to 10,000 με in tension (indicated in the scale by red for color images or white for grayscale). However, two thirds of the pixels presented deformations in a much narrower range between −4000 and +4000 με. The average strains in loading direction, obtained from the strain maps in ROIs 1, 2, 3, and 4, were −660, −266, −655, and −655 με, respectively. Thus, strain in the loading direction consistently indicated a compression field, despite measurements which indicate that sub-regions were experiencing tensile strain.

4.2.2. Creep and shrinkage in NSC

After the application of stress, images of the same ROI on the NSC were obtained after one and 28 days under loading and drying (in 50% RH conditions). For these analyses, the REF

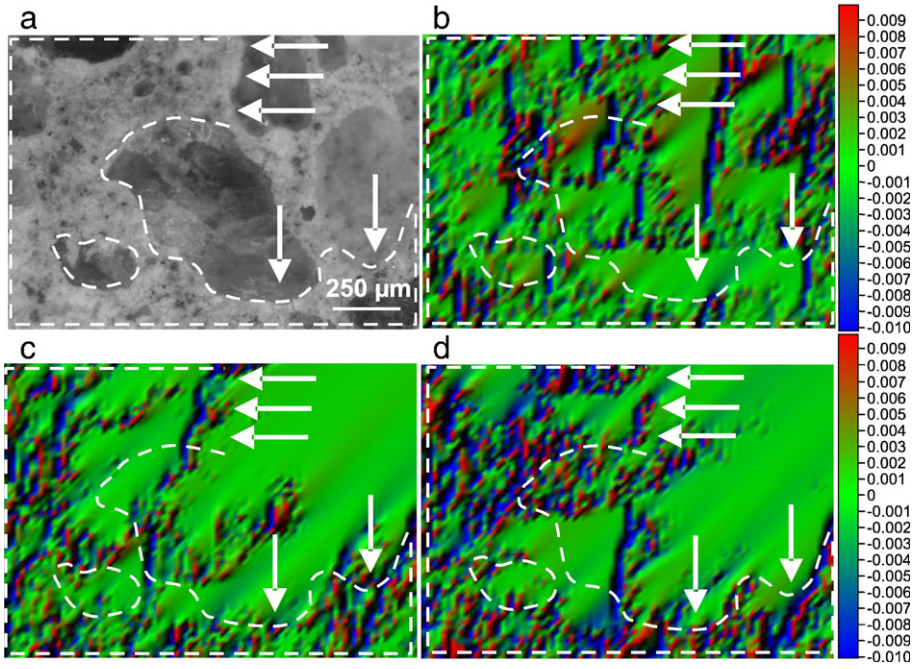

Fig. 7. (a) A representative region of interest (ROI 2), obtained at high magnification, on an NSC specimen under 9.7 MPa (1440 psi) stress; (b) Elastic strain map, (c) 1-day creep plus shrinkage strain map, (d) 28-day creep plus shrinkage strain map, for this ROI, in the loading direction, in mm/mm (in/in).

used was the image immediately after loading to eliminate elastic effects. Fig. 7c shows a representative strain map obtained after one day under sustained stress on ROI 2 at high magnification.

The displacement map for creep plus shrinkage after one day under testing (not shown here, but reported elsewhere [10]), showed pixels getting closer to one another in the loading direction, indicating a compression strain field. The average creep plus shrinkage strain from the strain map in Fig. 7c was −294 με which represents 110% of the average elastic strain obtained in the same ROI. The other three ROIs analyzed (i.e., ROIs 1, 3 and 4) had an average creep plus shrinkage strain of −440, −363, and −275 με, respectively. When comparing the creep plus shrinkage map at one day of testing (Fig. 7c) with elastic strain map (Fig. 7b), it can be seen that a non-uniform strain field is present in both; however, more intermediate values (indicated by a green in the color map or lighter gray in the grayscale map) were present in the strain map for creep plus shrinkage.

In addition, Fig. 7c shows a heterogeneous strain field with differences between aggregate-rich and paste-rich sub-regions, as indicated by the dashed lines and arrows. For instance, the left and bottom regions [surrounded by dashed lines and identified as paste-rich sub-regions, as seen in the actual image (Fig. 7a)], exhibited greater strain and more heterogeneous creep plus shrinkage deformation. In fact, the center and top-right regions, which correspond to three large aggregate particles (as seen in the ROI), show less heterogeneity in strain values; this results in a "smoother" area in the creep plus shrinkage strain map in Fig. 7c. This same strain map in Fig. 7c indicated a primarily compression field in this ROI at this age, although some areas undergoing tensile strains were also found as shown by the green-to-red (or lighter gray to white) parts of the map. The presence of sub-regions under tension suggests that even though the stress field is compressive, the heterogeneity of the microstructure resulted in a non-uniform stress distribution and, likely, stress concentrations. This type of non-uniformity has been observed by image analysis performed to micrographs obtained with environmental scanning electron microscopy in cement paste samples undergoing drying [7,8]. Those authors concluded that contraction due to shrinkage was the net result of both expanding and contracting regions.

After 28 days under loading and drying, the same ROI in this NSC sample was imaged again to produce the strain map shown in Fig. 7d. The same scale for strain has been used in Fig. 7c and d, to facilitate comparison of these maps obtained at 24 h and 28 days. As they represent the same ROI, similar features are noted in Fig. 7c and d. One key difference is in the average strain indicated in the maps at different times. After 28 days undergoing creep and shrinkage, the average strain increased from −294 to −1389 με. This increase can also be clearly observed in the left and bottom (paste-rich regions) where the 28-say strain map (Fig. 7d) shows green-to-blue regions in the color map (or darker gray in the print grayscale map), as compared to the 1-day strain map (Fig. 7c). The same trends were observed in the other ROIs for this sample. For instance, ROI 4, also taken at high magnification, had an average creep plus shrinkage strain of −275 and −1924 με after one and 28 days, respectively [10].

In addition to exhibiting greater average strain, at 28 days the time-dependent strains were less uniform and more variable than those measured at 24 h. The paste-rich left and bottom areas of the ROI in Fig. 7d (i.e. inside the dashed line) appear to concentrate most of the compressive deformations as well as greater variability in the measured strain.

In fact, the strain maps produced after one and 28 days both show greater strain in the paste-rich zones. For example, the average creep plus shrinkage strain considering only paste-rich sub-regions averaged −402 and −1879 με, at one and 28 days under testing, respectively. These values corresponded to 1.4 times the average creep plus shrinkage measured in the overall ROI (i.e., including paste and aggregate) at the same time of testing. Moreover, average strain in aggregate-rich zones at 28 days of tenting was −1003 με which was only 54% of that computed in the paste-rich zones. These measurements support the commonly held understanding that in NSC time-dependent strains occur primarily in the paste, while the stiffer, coarse aggregate, functions to restrain creep and shrinkage of the paste [14,28].

Because of the dissimilar creep plus shrinkage deformation between paste and aggregate-rich zones, it was concluded that the ITZ was subjected to high strains. In fact, the strain maps showed higher compressive deformations in some of the interfacial zones in this ROI, as indicated by the arrows in Fig. 7c and d.

In contrast, such dissimilar deformation between paste and aggregate-rich regions (as shown in Fig. 7c and d) was not observed for the elastic strains in the NSC (see Fig. 7b). While variability in the strains was clear from the elastic deformation maps, differences between aggregate and paste-rich regions were not as evident as those in the creep plus shrinkage maps. This might be due to the fact that elastic deformations in aggregate and paste depend on applied stress and their respective elastic moduli, while creep plus shrinkage deformations are phenomena occurring fundamentally in the paste.

In order to better visualize the heterogeneity of the creep plus shrinkage deformation, Fig. 8 shows the percentage of pixels showing high tensile strain (more than 2000 με), intermediate strain (between 2000 and 0 με and between 0 and −2000 με), and high compressive strains (less than −2000 με) after one and 28 days of testing. This analysis shows that the strain distribution in NSC clearly changes between one and 28 days

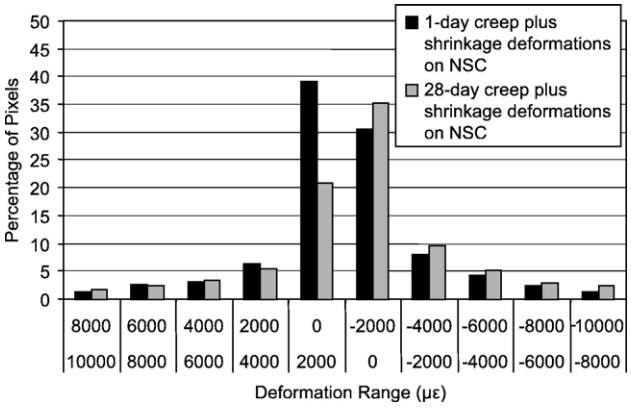

Fig. 8. Strain distribution after one and 28 days under loading and drying in NSC.

of testing, with the percentage of pixels showing strains in the intermediate range (between 2000 and −2000 με) decreasing from 70% after one day to 56% after 28 days. This decrease in the intermediate range was mainly compensated by an increase in the percentage of pixels in the high compressive strain range. Pixels showing high compressive strains (less than −2000 με) increased from 19% at one day to 27% at 28 days. Consequently, the average creep plus shrinkage strain became more negative, with averages of −294 and −1383 με after one and 28 days of testing, respectively. In addition, although both strain maps indicated pixels under both compression and tension, the percentage of pixels under compression was greater than those under tension.

Finally, not only does the average strain in NSC increase with time under loading and drying, the standard deviation does as well; in this case, the standard deviation changed from 3078 με at one day to 4983 με at 28 days. This could indicate the dissimilarity in behavior between aggregate and paste increases with time. That is, as NSC paste underwent longer durations of creep and shrinkage, larger differences in strain with respect to the aggregate were apparent. Consequently, the standard deviation of the strain, considering both phases, would increase.

4.3. Deformation in HPC

4.3.1. Elastic strain in HPC

The strain map for the elastic deformation in a ROI at high magnification (shown in Fig. 9a) in a HPC sample is presented in Fig. 9b. As with NSC, this strain map presents a heterogeneous elastic strain field, with some regions in tension, but with most of the ROI in compression. The average elastic strains from the strain map in ROI 2 (not shown here, but reported elsewhere [10]) and ROI 4 (in Fig. 9a) were −1480 and −1533 με, respectively.

Similarities are clearly evident between the strain map (Fig. 9b) and microstructural features in the actual ROI (Fig. 9a). For example, the coarse aggregate particle at the center of the ROI exhibited less strain and less heterogeneity in its elastic response than the surrounding paste. Two other sub-regions, in the upper-left, which also showed smaller and more uniform strain, correspond to two aggregate particles (Fig. 9a). The lower part of the strain map, which is paste-rich, indicates greater strain. This variation in elastic strain experience by the paste and aggregate, with the application of 28.4 MPa (4115 psi) stress, is likely due the dissimilarity in elastic properties between these two phases. This elastic mismatch could have induced microcracking at the ITZ, indicated by a narrow high-strain band adjacent to the coarse aggregate and denoted by arrows in Fig. 9b, as modeled previously [27].

4.3.2. Creep and shrinkage in HPC

For the analysis of time-dependent strains in HPC (as with NSC), images obtained immediately after loading were used as REF. Pattern matching was applied to compare REF with images obtained of HPC samples after one and 28 days under load in 50% RH conditions. An image of one of the HPC ROIs and the corresponding strain (i.e., creep plus shrinkage) maps are shown in Fig. 9a and c, respectively.

A heterogeneous strain field is clearly apparent in Fig. 9c, where the aggregate-rich sub-regions in the center and upper-right of the image appear “smoother” and exhibit less compressive strain than the paste fraction making up the remainder of the ROI. The creep and shrinkage map shows lower strain values (i.e., brighter green in the color image or

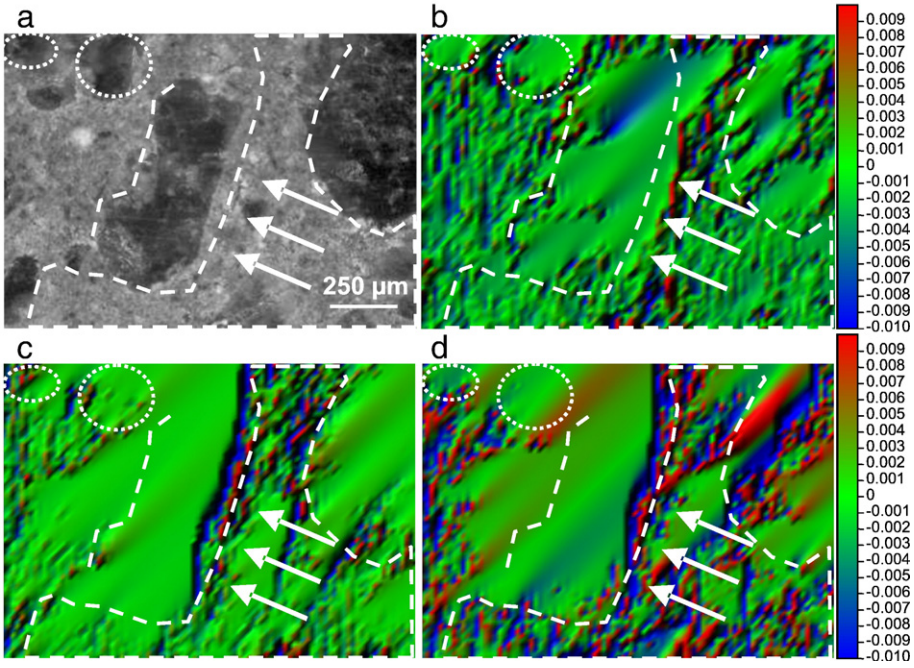

Fig. 9. (a) A representative region of interest (ROI 4), obtained at high magnification, on an HPC specimen under 28.4 MPa (4115 psi) stress; (b) Elastic strain map, (c) 1-day creep plus shrinkage strain map, (d) 28-day creep plus shrinkage strain map, for this ROI, in the loading direction, in mm/mm (in/in).

lighter gray in the grayscale image) than those in the elastic strain map for HPC (Fig. 9b).

One clear difference between the creep plus shrinkage and the elastic strain maps for HPC was observed. The "smoother" area at the center of the ROI in Fig. 9c seems to be larger than in Fig. 9b. In Fig. 9c, the lower strain region encompasses not only the aggregate, but some of the surrounding cementitious matrix as well; on average, the lower strain region on the creep plus shrinkage map was 145 μm larger than that on the elastic strain map. This may indicate an aggregate restraining effect on paste creep and shrinkage, as postulated by Pickett [28] and Neville [14]. In this case, it is proposed that the paste surrounding the aggregate is not as free to deform as paste farther from the aggregate.

On the other hand, a similar feature is apparent in the one-day creep plus shrinkage and elastic strain maps. In both maps, a region of high-strain is detected across the ROI, following the right edge of the aggregate particle at the center of ROI as pointed out by the arrows in Fig. 9c. This high-strain line may indicate cracking along the ITZ. It should be noticed that the high-strain zone shown in Fig. 9c does not include the elastic strain shown in Fig. 9b.

The strain maps generated from images of the same ROI after one (Fig. 9c) and 28 days (Fig. 9d) of loading and drying show similar features. However, the strain map after 28 days (Fig. 9d) shows strain values at the more extreme ends of the scale. This is represented by some red regions in tension and blue regions in compression, compared with more intermediate green colors in the strain map after one day (Fig. 9c). (For the printed grayscale figure, white regions indicate tension and black compression.) The average strain observed increased from −266 με at one day to −1136 με at 28 days.

As with NSC (Fig. 7c and d), the time-dependent strains in HPC were non-uniform across the ROIs examined. In the paste-rich sub-region, noted by dashed lines in the strain map (Fig. 9d), larger and more heterogeneous strains were apparent. Also, by comparing Fig. 9c and d, time-dependent strains increased between one and 28 days, with increases in strain particularly evident along the ITZ during this period. In general, strains in the HPC were greater in the regions with less coarse aggregate. The average creep plus shrinkage in the paste-rich zones was −2046 με, which is 80% higher than the strain of −1136 με measured in the paste and aggregate combined, indicating the paste is the predominant source of time-dependent strain in this HPC, as was the case for the NSC.

A frequency plot of the creep and shrinkage after one and 28 days, obtained from strain maps for HPC in Fig. 9c and d, is shown in Fig. 10. This comparison shows that as time under loading and drying increased, the number of pixels in compression also increased in this HPC. At one day of loading and drying, 78% of the pixel strains fell within the range +2000 and −2000 με, while at 28 days the range which contained 78% of the pixels was much broader, encompassing +6000 to −6000 με. Not only did the average strain increase from −266 to −1136 με, but the standard deviation also increased by a factor of 3.5. This increase in the standard deviation could reflect the greater time dependent strains in the paste relative to the aggregate. That is, as time under loading and drying increases the difference between strains in the paste and the aggregate fractions increased, leading to greater variability in the data. Thus, the increase in standard deviation in the strain measurements with time coupled with the observations of lower strain and more homogeneity in strain measurements in the coarse aggregate-rich subregions may be viewed together as an indication that the creep and shrinkage occur primarily in the HPC paste.

4.4. Comparison of creep and shrinkage behavior in NSC and HPC

The time-dependent strain maps obtained for NSC (shown in Fig. 7c and d) and HPC (shown in Fig. 9c and d) may be compared to better understand the underlying processes of creep and shrinkage deformation in these two types of concrete. Even though NSC and HPC used in this study are quite different in properties and mixture design, some comparisons can still be made because both ROIs shown in Figs. 7a and 9a were taken at the same magnification and contain similar content of coarse aggregate by area fraction.

Comparison of creep plus shrinkage strain maps shows differences in the strain measured in the aggregate and paste-rich zones in both the NSC and HPC. Also, generally higher compressive strains, denoted by darker blues, (or darker grays in the grayscale image) are noted at the ITZ (as pointed out by the white arrows) in both types of concrete.

At one day of creep and shrinkage, the NSC strain map (Fig. 7c) showed more heterogeneity than its HPC counterpart (Fig. 9c). This is especially apparent in the paste-rich zones, which are indicated by the dashed line. In the NSC strain map, more "texture" or variation is noticed in the paste-rich regions, indicating sharper changes in deformation across the paste-rich subregions.

After 28 days of creep and shrinkage, the strain maps for both the NSC (Fig. 7d) and HPC (Fig. 9d) show overall higher compressive strain, as denoted by darker blues (or darker grays in the grayscale image).

When comparing the paste-rich regions (left and bottom on both ROIs), it can be observed that the normal strength paste exhibited higher strain values than the high performance paste.

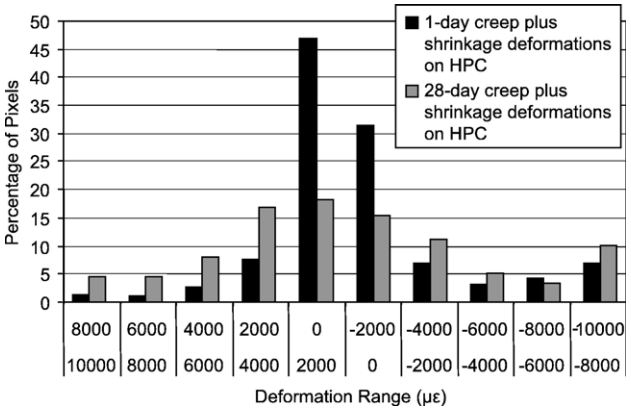

Fig. 10. Strain distribution after one and 28 days under loading and drying in HPC.

HPC shows less heterogeneity in its strains, as evidenced by the smoother appearance of the paste rich zones. However, the high strain area along the ITZ in HPC (located in the center of the map) would suggest the presence of local damage in HPC probably initiated during elastic deformation, as noted previously.

NSC exhibited greater creep plus shrinkage strains than HPC at both one and 28 days of loading and drying, despite its longer curing period. The average strain when comparing the values for NSC and HPC differed by only 28 με at one day and by 247 με after 28 days. That is, the differences between the two mixtures increased with time. The greater creep plus shrinkage observed in NSC it is believed to be a consequence of the properties of the paste fraction, since both ROIs had comparable aggregate fractions and both concretes were produced with the same aggregate.

The standard deviation of creep plus shrinkage strains after one day of testing was 5575 με for NSC and 4938 με for HPC. The lower variability in creep measured in the HPC is presumed to be a consequence of the more uniform microstructure in the HPC paste fraction as compared to the NSC paste microstructure. It is proposed, that as anticipated, the presence of fly ash, silica fume and superplasticizers in the HPC mixture improved the homogeneity of the paste fraction and lead to the observed decreased variation in creep [29].

In addition, the lower creep observed in the HPC might be also related to reduced mismatch in the deformation occurring in the paste and aggregate fractions, which, thus, would decrease the overall variability in HPC creep. In contrast, NSC showed greater variability due, in part, it is proposed to greater mismatch in creep behavior of the NSC paste and aggregate.

Another way to visualize the differences between deformation in aggregate-rich and paste-rich areas in NSC and HPC is by obtaining strain profiles along trace lines. Fig. 11 shows strain profiles obtained along 800-μm (0.031-in) straight lines which cross over the ITZ in 28-day creep plus shrinkage strain maps for NSC and HPC. Fig. 11 also shows the ROIs and the location of the traces. Both strain profiles show the heterogeneous creep plus shrinkage present in NSC and HPC mixtures. They also show that most of the strains are compressive, as previously observed in the separate analyses of strains maps for NSC and HPC.

The strain profile for NSC shows that the strain in the coarse aggregate is characterized by a relatively even trace, as seen at the 200 μm lengths at the beginning and at the end of the strain profile in Fig. 11a. Further away from the aggregate, in the center portion of the trace, the values show sharp changes and much unevenness. There are two narrow portions, identified as "high strain zone" in the figure, where the change in strain is the greatest. Those high strain zones are approximately 200 μm away from the ends of the test line which is the vicinity of the aggregate/paste interface, as seen in the actual ROI. The high strain zone likely indicates damage in this region due to strain mismatch between aggregate and paste.

The thickness of this high strain sub-region NSC averaged 210 μm (0.0083 in) after 28 days under loading and drying. This average corresponds to that obtained from six trace lines drawn across the ITZ. The thickness of this high strain region is about four times the upper bound of ITZ thickness found in concrete [30], which might indicate that damage due to strain mismatch has an influence beyond the physical presence of the ITZ.

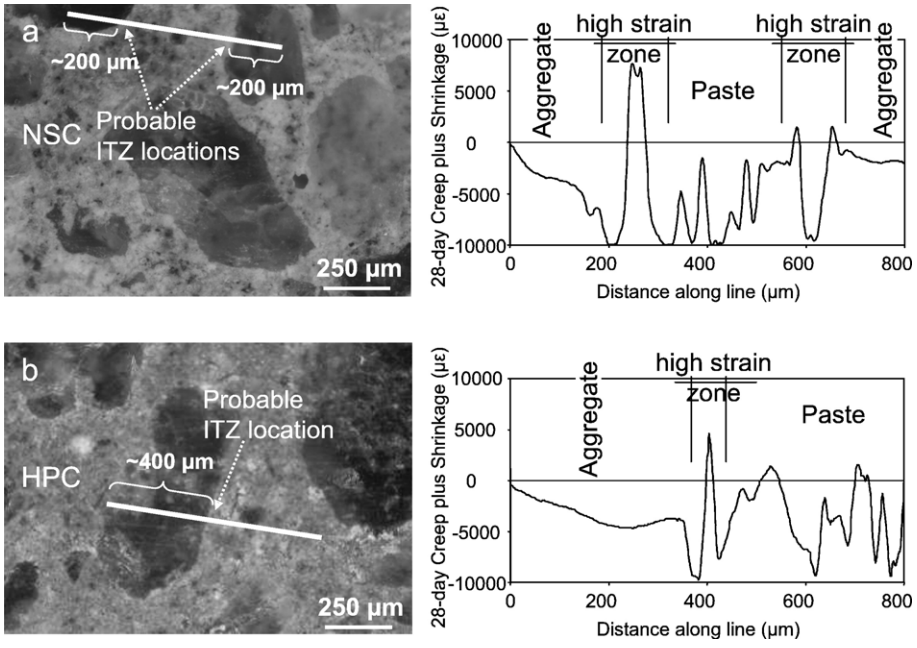

Fig. 11. (a) Representative deformation maps for specific creep in the loading direction after 28 days of loading and location of the test line in NSC. (b) Strain profile along test line in NSC. (c) Representative deformation maps for specific creep in the loading direction after 28 days of loading and location of the test line in HPC. (d) Strain profile along test line in HPC.

The strain profile for HPC (Fig. 11b) shows some similar features. For example, the aggregate, which covers approximately the first 400 μm of the strain profile, shows a smooth strain variation while the paste, present in the second 400 μm of the strain profile, shows relatively more uneven strains. The high strain zone is present in the vicinity of the ITZ. However, one difference between the strain profiles for the HPC and for NSC (Fig. 11a), is that in HPC the thickness of the high strain zone measures 103 μm (0.004 in) at 28 days of testing; this is about half the thickness of the high strain zone in the NSC. This might indicate that the strain mismatch in the ITZ is more important in describing the creep and shrinkage behavior in NSC and considerably less important in HPC.

5. Conclusions

Deformation in normal strength and high performance concrete during creep and shrinkage were compared through bulk measurements of strain and by the novel application of image analysis by digital image correlation. The imaging procedure developed provided visual confirmation the much commonly held understanding of the relationships between the structure of normal strength and high strength concrete and elastic and time-dependent deformations. In particular, the strain maps generated by this technique provides quantitative data linking the structure and deformation, leading to improved understanding of the influence of the aggregate/paste interface in NSC and HPC in localized creep and shrinkage. Key outcomes include these findings:

- For both NSC and HPC, elastic strain was found to be heterogeneously distributed in the cement paste and aggregates, providing both quantitative and qualitative (i.e., visual) confirmation of anticipated behavior. High-strain sub-regions along the aggregate/paste interface (or in the vicinity of the ITZ) were observed in both types of concrete, presumably due to differences in stiffness between the paste and the aggregate.
- The maps for elastic and time-dependent strain, obtained by image analysis, showed some similarities to the actual phases and structure in the images of the region of interest (ROI), indicating larger and more heterogeneous strain in the paste fraction than in the coarse aggregate particles for both NSC and HPC.
- Deformations resulting from creep plus shrinkage, while under constant stress in 50% RH conditions, were found to be highly heterogeneous in both NSC and HPC. As the time under loading and drying increased, both the average strain and the standard deviation of these measurements increased in the ROIs examined in each concrete type. Because the non-uniformity was concentrated in the paste-rich fractions, the increase in non-uniformity with time suggests that creep and shrinkage are phenomena primarily occurring in the paste in both NSC and HPC.
- As a consequence of this dissimilar deformation in the aggregate and paste, the largest strain and the largest variation in strains were typically measured in the vicinity of the ITZ for both NSC and HPC.
- When compared with NSC, HPC exhibited smaller creep plus shrinkage deformation and less heterogeneity in strain distribution. Since the same aggregate was used in both mixtures, it can be concluded that the reduced creep plus shrinkage and heterogeneity resulted from the greater homogeneity in the HPC paste fraction as compared to NSC.
- It is believed that the reduction in the deformation mismatch between aggregate and paste afforded by the reduced creep plus shrinkage of the HPC paste might have decreased the thickness of the high strain sub-region at the ITZ in HPC. In this research, the high strain zone thickness was two times greater in NSC, which suggests that strain mismatch in the ITZ is significantly more important in describing the creep and shrinkage behavior in NSC and considerably less important for HPC.

Acknowledgements

The authors gratefully acknowledge the research support from the Georgia Department of Transportation under Georgia DOT research project no. 2041, Task Order no. 02-06. The conclusions expressed herein are those of the authors and do not necessary represent the opinions or conclusions of the Georgia Department of Transportation. The insights on image analysis given by Dr. Arun Gokhale in the School of Materials Science and Engineering at Georgia Tech and the help of Alan Mullenix with preparing the test setup are greatly appreciated.

References

[1] A.M. Neville, W.H. Dilger, J.J. Brooks, Creep of plain and structural concrete, Construction Press, 1983.
[2] Z.P. Bazant, Prediction of concrete creep and shrinkage: past, present and future, Nuclear Engineering and Design 203 (1) (2001) 27–38.
[3] ACI Committee 209, Prediction of creep, shrinkage, and temperature effects in concrete structures, ACI Manual of Concrete Practice, American Concrete Institute, Farmington Hills, MI, 1997, p. 47.
[4] Comite Euro-Internacional du Beton (CEB) and Federation Internationale de la Precontrainte (FIP), Evaluation of the Time Dependent Behavior of Concrete. 1990, Lancaster: The Construction Press.
[5] J.S. Lawler, D.T. Keane, S.P. Shah, Measuring three-dimensional damage in concrete under compression, ACI Materials Journal 98 (6) (2001) 465–475.
[6] S. Choi, S.P. Shah, Measurement of deformations on concrete subjected to compression using image correlation, Experimental Mechanics 37 (3) (1997) 307–313.
[7] C.M. Neubauer, H.M. Jennings, The use of digital images to determine deformation throughout a microstructure – Part II – Application to cement paste, Journal of Materials Science 35 (22) (2000) 5751–5765.
[8] C.M. Neubauer, H.M. Jennings, E.J. Garboczi, Mapping drying shrinkage deformations in cement-based materials, Cement and Concrete Research 27 (10) (1997) 1603–1612.
[9] C.M. Neubauer, T.B. Bergstrom, K. Sujata, Y. Xi, E.J. Garboczi, H.M. Jennings, Drying shrinkage of cement paste as measured in an environmental scanning electron microscope and comparison with microstructural models, Journal of Materials Science 32 (24) (1997) 6415–6427.
[10] M. Lopez, Creep and shrinkage of high performance lightweight concrete a multi-scale investigation, School of Civil and Environmental Engineering, Georgia Institute of Technology, Atlanta, GA, 2005, p. 531.
[11] M. Lopez, K.E. Kurtis, L.F. Kahn, Creep strain distribution and deformation mechanisms of high performance lightweight concrete, Advances in Cement and Concrete, Engineering Conferences International, Copper Mountain, Colorado, 2003.

[12] G.E. Troxell, J.M. Raphael, R.E. Davis, Long-term creep and shrinkage tests of plain and reinforced concrete, Cement and Concrete, ASTM Proceedings, Los Angeles, 1958.
[13] G. Pickett, Effect of aggregate on shrinkage of concrete and hypothesis concerning shrinkage, Journal of the American Concrete Institute 27 (5) (1956) 581–590.
[14] A.M. Neville, Creep of concrete as function of its cement paste content, Magazine of Concrete Research 16 (46) (1964) 21–30.
[15] F. de Larrand, P. Acker, R. Le Roy, Shrinkage creep and thermal properties, in: S.P. Shah, S.H. Ahmad (Eds.), High Performance Concrete: Properties and Applications, McGraw-Hill, New York, NY, 1994, pp. 65–114.
[16] W.H. Dilger, C. Wang, Creep and shrinkage of high-performance concrete, The Adam Neville Symposium: Creep and Shrinkage — Structural Design Effects, SP-194, American Concrete Institute, Atlanta, 2000.
[17] M. Buil, P. Acker, Creep of a silica fume concrete, Cement and Concrete Research 15 (3) (1985) 463–466.
[18] A.S. Ngab, A.H. Nilson, F.O. Slate, Shrinkage and creep of high-strength concrete, Journal of the American Concrete Institute 78 (4) (1981) 255–261.
[19] ASTM C 512, Standard Test Method for Creep of Concrete in Compression, American Society for Testing and Materials, West Conshohocken, PA, 2002.
[20] Matrox-Imaging, Matrox Inspector 4.1. 2002.
[21] J.B. Kennedy, A.M. Neville, Basic statistical methods for engineers and scientists, 2d ed., Crowell, 1976, p. 490.
[22] J. Neter, M.H. Kutner, C. Nachtsheim, W. Wasserman, Applied linear statistical models, 4th ed., WCB McGraw-Hill, 1996, p. 1408.
[23] ASTM C 191, Standard Test Method for Time of Setting of Hydraulic Cement by Vicat Needle, American Society for Testing and Materials, West Conshohocken, PA, 2004.
[24] ASTM C 39, Standard Test Method for Compressive Strength of Cylindrical Concrete Specimens, American Society for Testing and Materials, West Conshohocken, PA, 2004.
[25] M. Lopez, L.F. Kahn, Prestress losses in high performance lightweight concrete pretensioned bridge girder, PCI Journal 50 (5) (2005) 84–94.
[26] M. Lopez, L.F. Kahn, K.E. Kurtis, Creep and shrinkage of high-performance lightweight concrete, ACI Materials Journal 101 (5) (2004) 391–399.
[27] T.W. Bremner, T.A. Holm, Elastic compatibility and the behavior of concrete, Journal of the American Concrete Institute 83 (2) (1986) 244–250.
[28] G. Pickett, Effect of aggregate on shrinkage of concrete and hypothesis concerning shrinkage, Journal of the American Concrete Institute 27 (5) (1956) 581–590.
[29] P.C. Aïtcin, High-Performance Concrete, E. & F.N. Spon, London, 1998, p. 591.
[30] P.K. Mehta, P.J.M. Monteiro, Concrete: Microstructure, Properties, and Materials, 2nd ed., McGraw-Hill, 1993.